RESEARCH ARTICLE

Key Points:
- During low winds, a one-dimensional momentum balance describes the hydrodynamics at a channel bend
- Tidal asymmetry in along-channel flows may be related to tidal asymmetry in the lateral sea-surface gradient
- Cross-channel winds drive subtidal changes to the magnitude and vertical structure of cross-channel flows

Correspondence to:
A. Wargula,
wargula@usna.edu

Curvature- and Wind-Driven Cross-Channel Flows at an Unstratified Tidal Bend

Anna Wargula[1] [iD], Britt Raubenheimer[2] [iD], and Steve Elgar[2] [iD]

[1]United States Naval Academy, Annapolis, MD, USA, [2]Woods Hole Oceanographic Institution, Woods Hole, MA, USA

Abstract Observations of currents, water levels, winds, and bathymetry collected for a month at an unstratified, narrow (150 m), shallow (8 m), 90° tidal inlet bend are used to evaluate an analytical model for curvature-driven flow and the effects of local wind on the cross-channel circulation. Along-channel flows ranged from −1.0 to 1.4 m/s (positive is inland), and the magnitudes of cross-channel flows were roughly 0.1–0.2 m/s near the outer bank of the bend. Cross-channel observations suggest the lateral sea-surface gradients and along-channel flows are tidally asymmetric and spatially variable. The depth-averaged along-channel dynamics are consistent with a balance between the surface tilt and centrifugal acceleration. The vertical structure and magnitude of cross-channel flows during weak winds are consistent with a one-dimensional depth-varying balance between centrifugal acceleration, bottom stress, and diffusion. Low-passed (to remove tides) surface and bottom cross-channel flows are correlated ($r^2 = 0.5$–0.7) with cross-channel wind velocity, suggesting that winds can enhance or degrade the local-curvature-induced, two-layer flow and can drive three-layer flow. The observed flow response to the wind is larger than that expected from a one-dimensional balance, suggesting that two-dimensional and three-dimensional processes may be important.

1. Introduction

Cross-channel flows laterally redistribute water properties and momentum, affecting along-channel dynamics (Lerczak & Geyer, 2004), longitudinal dispersion (Lacy & Monismith, 2001; Seim & Gregg, 1997), and bay-ocean exchange (Smith, 1976). Thus, curvature-driven cross-channel flows (e.g., at a bend or headland) have been studied for many years (Boussinesq 1868; Geyer 1993; Kalkwijk & Booij, 1986; Rozovskii, 1957; Thomson 1876).

At an unstratified bend, centrifugal forcing of flow causes helical particle motions with a primary along-channel (streamwise) flow and secondary cross-channel (stream-normal) flow toward the outside of the bend at the surface and toward the inside of the bend near the bed ("two-layer flow") (Kalkwijk & Booij, 1986). Field and laboratory studies suggest that upstream geometry (e.g., an upstream headland or bend) can cause tidal asymmetry in the development of cross-channel flows inside a bend (Vennell & Old, 2007), as well as flow decelerations and adverse sea-surface tilts at the outer bank of a downstream bend (Blanckaert, 2010). Tidal asymmetry of cross-channel flows has been identified as a major driver of residual estuarine circulation in stratified systems (Becherer et al., 2015; Chant & Wilson, 1997; Lerczak & Geyer, 2004). However, the importance of tidal asymmetry and lateral variability in flows and bathymetry to the cross-channel dynamics in an unstratified inlet are not understood.

Winds can drive subtidal changes to inlet circulation on local (Wong & Valle-Levinson, 2002) and large (Wong, 1994) length scales. Numerical and observational studies suggest that although local wind effects occur over a small area, they can influence overall dynamics substantially by driving flows (Csanady, 1973; Hearn et al., 1987; Huijts et al., 2009; Li & Li, 2012; Mathieu et al., 2002) and pressure gradients (Hinata et al., 2010), modifying circulation patterns (Ponte et al., 2012), increasing shear (MacVean & Lacy, 2014), and enhancing sediment transport and morphological evolution (Chen et al., 2009). Local winds indirectly can affect cross-channel dynamics either owing to Ekman dynamics (Sanay & Valle-Levinson, 2005; Winant, 2004) or by driving lateral phase lags in along-channel flows, which generate cross-channel flows via differential advection or cross-channel baroclinic forcing (Chen et al., 2009; Waterhouse & Valle-Levinson, 2010; Li & Li, 2012; Wong, 1994; Xie et al., 2017). However, there are few studies of the direct effects of local winds on cross-channel flows in shallow (e.g., less than Ekman depth), unstratified systems.

Here, in situ measurements of currents, water levels, winds, and bathymetry at an unstratified tidal inlet bend are used to evaluate a laboratory-tested analytical model for curvature-driven flow (Kalkwijk & Booij, 1986) and the effects of local winds on the cross-channel circulation and dynamics.

2. Field Observations

2.1. Site Location

New River Inlet is ∼100 km south of Cape Hatteras, on the coast of North Carolina, USA. The inlet width is 1,000 m at the mouth and tapers to 200 m about 800 m inland from the mouth, where two sharp 90° bends form the shape of a reversed "S" (Figure 1c). New River extends about 25 km upstream from the inlet, and the backbay has an area of about 68 km^2 (MacMahan et al., 2014). Approximately 3 km upstream from its mouth, the inlet intersects the Intracoastal Waterway, which continues north and south from New River, connecting to many additional inlets, including Browns Inlet (located 12 km to the north) and New Topsail Inlet (located 36 km to the south).

The bathymetry was surveyed (relative to NAVD88) five times (16–17 April; 1–2, 10–11, 17–18, and 25 May 2012). Temporal changes in the sand levels near the profiler (Figure 1a, black open circle) inside the inlet channel were less than 0.2 m, and the results are not sensitive to which bathymetry survey is used. Here the bathymetry surveyed during the middle of the study period (from 10 to 11 May) is used.

There are two channels inside the inlet mouth that converge at the bend. There is a western channel (hereinafter referred to as the "deep channel") (50–100 m wide, 8 m deep near the bend, decreasing to
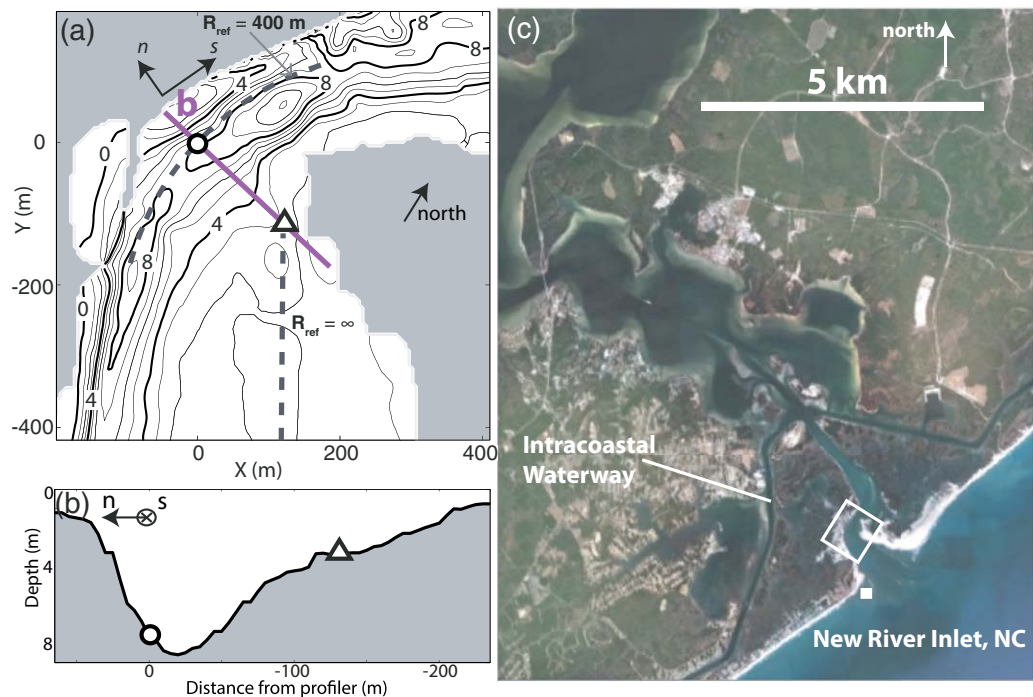

Figure 1. (a) Contours of bathymetry (1 m depth increments with 0, 4, and 8 m contours thicker and labeled) overlaid with locations of the colocated current profiler and pressure gage (black open circle) and the pressure gage (black open triangle). The black dashed curve (radius R_{ref} = 400 m) and line (R_{ref} = ∞) are included for reference. Positive along-channel and cross-channel directions are indicated with black arrows labeled s and n. Gray regions correspond to unsurveyed areas (see Figure 1c for true shoreline). (b) Depth (black solid curve) versus cross-channel distance from the profiler (positive to the left (west)) along the purple line labeled b in Figure 1a. Instrument locations are indicated by the black open circle and triangle. Flood and positive cross-channel flow directions (positive s and n) are into the page (indicated by a symbol ×) and to the left (indicated with an arrow). (c) Google Earth image of the North Carolina coast showing New River Inlet and the Intracoastal Waterway. The white open square shows the location of Figure 1a. The white filled square is the location of onsite wind measurements.

approximately 5 m deep near the inlet mouth) and an eastern channel on the shallow shoals (hereinafter referred to as the "shoals channel") (2–3 m deep). The western channel was dredged in April 2012.

The radius of curvature R is defined as the change in angle along a streamline $R=-\partial s/\partial \theta$, where s is the along-streamline coordinate and θ is the angle of the streamline (Hench et al., 2002). Typically, a radius of curvature is estimated using the arc between the inflection points in the geometry of a channel bend along the centerline of either the channel or the thalweg (the deepest part of the channel) (Elston, 2005). However, the local radius of curvature can vary spatially and tidally owing to sharp gradients in the local geometry and deviations of the flow from the geometry. The shoals channel nearly is straight (Figure 1a, vertical dashed line). The deep channel has a "bend-scale" (from bend inlet to bend outlet) curvature of 400 m, which approximately aligns with the local contours near the profiler (Figure 1a, compare contours near black open circle with the dashed curve).

2.2. Water Level and Flow Observations

Water levels and currents were measured at the bend (Figure 1a, symbols) nearly continuously during May 2012. Water levels were measured at 2 Hz for 3,072 s starting on the hour with stand-alone pressure gages (Figure 1a, symbols). On the shoals (Figure 1a, black open triangle), the pressure gage was buried about 0.10 m below the seafloor to avoid dynamic pressure fluctuations (Raubenheimer et al., 2001), whereas the pressure gage in the deep channel was mounted on the seafloor (Figure 1a, black open circle). Pressure gage elevations were adjusted as needed to maintain roughly constant elevation with respect to sand level. These shifts in vertical location are accounted for in processing. Pressure measurements were corrected for atmospheric pressure fluctuations, measured at ground level about 5 km inland. Water depths were estimated from the near-seafloor pressure measurements assuming hydrostatic pressure and a water density ρ_0 of 1,024 kg/m^3 (the time-averaged measured density). Mean water levels η were estimated with respect to NAVD88 from the mean water depths h averaged over each 3,072 s record) and the bathymetry. The cross-channel pressure gradient estimated between the standalone pressure gages (Figure 1b, symbols) was referenced to a flat datum by assuming a flat water surface across the channel at slack tide (i.e., when the dominant centrifugal forcing is zero; Nidzieko et al., 2009). Results without this correction are qualitatively similar (Appendix A).

The pressure sensor in the deep channel (Figure 1a, black open circle) was colocated with an upward-looking Acoustic Doppler Current Profiler. Currents were measured in 0.50 m vertical bins from about 0.80 m above the bed to about 1.0–1.5 m below the water surface every minute for 12 min ending on the half hour and hour. Measured currents were averaged over hourly periods and extrapolated to the bed using a logarithmic fit assuming a no-slip condition, and to the surface using a parabolic fit assuming a no-shear condition (Geyer et al., 2000). As a result, near-bottom velocities may be underestimated or overestimated owing to uncertainty in the shape of the bottom boundary layer, and wind effects on currents may be underestimated near the surface.

Currents were rotated to streamwise and stream-normal directions (Figure 1a, coordinate system). There may be small errors in the rotation angle owing to inaccuracies in velocity measurements or extrapolation schemes. However, the results are not sensitive to $O(10°)$ changes in rotation. Temporal fluctuations in the along-channel angle were less than $\pm 10°$ from the principal axis of the flows (19° east of north; Emery & Thomson, 2001), and results are similar for fixed and temporally varying coordinate systems.

Boat-mounted current profiles along cross-channel transects near the in situ profiler (Figure 1a, black open circle) were obtained hourly for 10 h on 21 May to sample the lateral variability in water levels and currents from before to after maximum ebb. Boat velocity, position, and altitude above mean sea level (water levels) were measured at 1 Hz by GPS with real-time kinematic corrections. The downward-facing transducer was positioned 0.20 m below the water surface and sampled flows at 1 Hz with vertical bins from 0.02 to 0.50 m and blanking distances of 0.20 to 0.50 m, depending on the water depth (measured by a separate vertical acoustic beam) and velocity conditions. The water levels and depth-averaged current profile transects were averaged in time every 6 s (an equivalent of horizontally averaging over ~5 m). The averaged water levels were smoothed with a 30 point moving average.

2.3. Wind and Density Observations

Winds were measured (5 min means) from 28 April to 21 May with a wind-vane-type anemometer ~3 m above NAVD88 in 2 m water depth southwest of the inlet mouth (Figure 1c, white filled square). Hourly
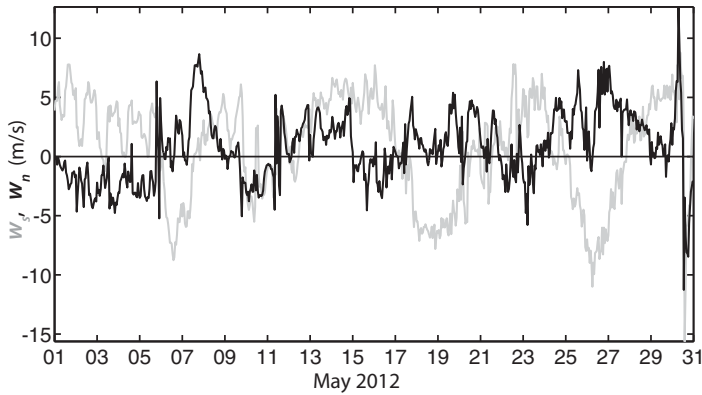
Figure 2. The local (Figure 1c, white square) along-channel (gray curve) and cross-channel (black curve) wind velocities (w_s, w_n) versus time.

offshore winds from a buoy in 10 m water depth 55 km southwest of New River Inlet (NDBC station 41038, location not shown) were used to extend the dataset. The onsite and NDBC wind measurements were correlated ($r^2 \sim 0.7$) with 95% confidence. Measured winds were converted to 10 m winds assuming a logarithmic layer, neutral stability, and a roughness length $z_0 = \alpha u_*^2 / g$ (Charnock, 1955), where α is an empirical parameter, u_* is the friction velocity, and g is gravitational acceleration. The results are not sensitive to variations in α over the range $0.008 < \alpha < 0.070$ (Brown & Wolf, 2009; Kraus, 1972; Peña & Gryning, 2008; Sempreviva et al., 1990; Smith, 1980).

Not including major storms, wind speeds ranged from 0 to 8 m/s, and most frequently were from the south or southwest. During tropical storm Alberto (Figure 2, 26 May), wind speeds were 10 m/s from the northeast and during tropical storm Beryl (Figure 2, 30 May), the wind speeds initially were 15 m/s from the southeast, and then rotated to be from the northwest. The local wind velocity at the bend may veer $O(10°)$ from those measured at the inlet mouth (D. Ortiz-Suslow, personal communication, 2015). However, the comparisons of cross-channel winds with currents are not sensitive to $\pm 20°$ variations in the local wind direction.

Temperature and salinity were measured with a conductivity-depth-temperature (CTD) sensor on 21 cross-channel transects near the bend (Figure 1a) at different tidal stages (flood/ebb/slack, spring/neap) from 1 to 20 May. Instrument noise is $O(0.1 \text{ kg/m}^3)$ (T. Lippmann, personal communication, 2014).

Depth-averaged and cross-inlet-averaged water density varied in time from roughly 1,023 to 1,025 kg/m³. Cross-channel changes in density were small (less than ~0.2 kg/m³, which is only slightly larger than the instrument accuracy), and vertical density variations usually were smaller than horizontal variations. The baroclinic pressure gradient is small (less than $O(10^{-4})$ m/s²), except near slack (not shown). Richardson numbers estimated from the velocity measurements in the deep channel (Figure 1a, black open circle) and from 52 density profiles collected within 50 m of the current profiler were less than 0.25 (not shown), except during slack tide, suggesting that mixing dominates over stratification, and that stratification should have little influence on the vertical structure of the flow (Geyer, 1993). Transient, larger horizontal gradients in density may occur in New River Inlet owing to occasional export of brackish water from the southern arm of the Intracoastal Waterway (J. MacMahan, personal communication, 2016). Thus, baroclinicity may have a transitory contribution to the dynamics that is not resolved with the available data set. The inlet is considered unstratified, and effects from density variations are neglected.

3. Theory

A streamwise coordinate system is adopted (hereinafter called along-channel and cross-channel directions, Figure 1a, coordinate system labeled s and n), such that the depth-averaged cross-channel flows are always zero. In contrast to prior studies (Geyer, 1993; Nidzieko et al., 2009), the sign of the along-channel flow is retained (positive (negative) during flood (ebb)) to avoid artificial M4 (6.2 h period overtide) frequency fluctuations in the time series and artificial M2 (12.4 h period lunar tide) fluctuations in the wind when rotated into the same reference frame. Assuming advection owing to cross-channel gradients in flow curvature, vertical advection, and horizontal diffusion are small (Hench et al., 2002; Kalkwijk & Booij, 1986), the cross-channel momentum balance at an unstratified bend in streamwise coordinates is (Geyer, 1993; Kalkwijk & Booij, 1986; Nidzieko et al., 2009):

$$\frac{\partial u_n}{\partial t} + u_s \frac{\partial u_n}{\partial s} + u_n \frac{\partial u_n}{\partial n} - \frac{u_s^2}{R} + f u_s = -g \frac{\partial \eta}{\partial n} + \frac{\partial}{\partial z}\left[A \frac{\partial u_n}{\partial z}\right] \tag{1}$$

where t is time, s and n are the along and cross-channel coordinates (positive into the inlet and to the outer (western) bank, Figure 1a, coordinate system), u_s and u_n are the along-channel and cross-channel velocities, R is the radius of curvature, f is the Coriolis parameter, η is the water level, and A is the vertical eddy viscosity. The left-hand side of equation (1) is (from left to right): local acceleration owing to the time rate of

change in cross-channel flows, along-channel advective acceleration owing to spatial adjustment of the cross-channel flows, cross-channel advective acceleration of the cross-channel flows, centrifugal acceleration owing to channel curvature, and Coriolis acceleration owing to rotation. These accelerations are balanced (right-hand side of equation (1), from left to right) by a cross-channel pressure gradient owing to a sea-surface tilt and vertical diffusion. The depth-averaged (indicated by the overbars) momentum balance based on equation (1) is:

$$\overline{u_s \frac{\partial u_n}{\partial s}} + \overline{u_n \frac{\partial u_n}{\partial n}} - \overline{\frac{u_s^2}{R}} + f\overline{u_s} = -g\frac{\partial \eta}{\partial n} + \overline{\frac{\partial}{\partial z}\left[A\frac{\partial u_n}{\partial z}\right]} \tag{2}$$

By definition, $\overline{u_n} = 0$ (thus, the depth-averaged local acceleration (not shown in equation (2)) is zero). The depth-average of vertical diffusion (equation (2), right-hand side) is defined as the difference between the surface (wind) and bottom boundary stress (Kalkwijk & Booij, 1986):

$$\overline{\frac{\partial}{\partial z}\left[A\frac{\partial u_n}{\partial z}\right]} = \frac{1}{h}\int_h^\eta \frac{\partial}{\partial z}\left[A\frac{\partial u_n}{\partial z}\right]dz = \frac{\tau^{sn}}{\rho_0 h} - \frac{\tau^{bn}}{\rho_0 h} \tag{3}$$

where h is the water depth and τ^{sn} and τ^{bn} are the cross-channel components of the surface (wind) $(z = \eta)$ and bottom $(z = h)$ boundary stresses, respectively. The wind stress is parameterized as $\tau^{sn} = \rho_a C_w w_n |W|$, where ρ_a is the density of air, C_w is the wind drag coefficient (Large & Pond, 1981), w_n is the cross-channel component of wind velocity, and $|W|$ is the total wind speed at 10 m above the water surface. Variability in the nearshore wind drag coefficient owing to waves, horizontal variability in currents, and topography are neglected (Ortiz-Suslow et al., 2015). Neglecting these effects may cause underestimation of the wind drag coefficient (Ortiz-Suslow et al., 2015) (section 4.3). The bottom stress is approximated as $\tau^{bn} = \rho_0 C_D u_{n,b}|U_b|$, where C_D is the bottom drag coefficient, $u_{n,b}$ is the near-bottom (defined here as velocity at $z = 0.8$ m, the measurement lowest in the water column) cross-channel velocity, and $|U_b|$ is the near-bottom total velocity magnitude ($|U_b| = \sqrt{u_{s,b}^2 + u_{n,b}^2}$).

The depth-varying and time-varying cross-channel momentum balance is obtained by subtracting equation (2) from equation (1), and substituting in equation (3) (Geyer, 1993; Kalkwijk & Booij, 1986; Nidzieko et al., 2009):

$$\frac{\partial u_n}{\partial t} + \left(u_s\frac{\partial u_n}{\partial s} - \overline{u_s\frac{\partial u_n}{\partial s}}\right) + \left(u_n\frac{\partial u_n}{\partial n} - \overline{u_n\frac{\partial u_n}{\partial n}}\right) - \frac{u_s^2 - \overline{u_s^2}}{R} + f(u_s - \overline{u_s}) = \frac{\partial}{\partial z}\left[A\frac{\partial u_n}{\partial z}\right] - \frac{\tau^{sn}}{\rho_0 h} + \frac{\tau^{bn}}{\rho_0 h} \tag{4}$$

Slack tide, the ∼30 min transition period between flood and ebb, is neglected in the momentum balance analysis. The first term, local acceleration, is neglected because it is small ($O(10^{-5})$ m/s^2) except near slack. The Rossby number is large (Ro = $U/(fR) \sim 50$, Nidzieko et al., 2009) inside the inlet owing to the sharp curvature. Thus, the Coriolis term is small ($O(10^{-5}$ to $10^{-4})$ m/s^2) compared with the dominant terms ($O(10^{-3})$ m/s^2), and is neglected. Wind stress also is relatively small ($O(10^{-5}$ to $10^{-4})$ m/s^2) and the tidal dynamics analysis here (sections 4.1 and 4.2) focuses on low wind cases. Bottom stress also is small ($O(10^{-4})$ m/s^2) relative to other depth-averaged terms (Nidzieko et al., 2009).

The nonlinear advection terms (equation (4), second and third parentheses on the left-hand side) are neglected in the analytical model (Kalkwijk & Booij, 1986) by assuming the length scales of flow adaptation are short compared with the length scale of variability in the curvature along the channel. Assuming a bottom drag coefficient C_D of 0.005 (Chen et al., 2014; Wargula et al., 2014), the adaptation length scale is $L_{adapt} = 11h$ (Kalkwijk & Booij, 1986), roughly 100 m, suggesting that the cross-channel flows have adapted to the curvature near the mid-point of the ∼400 m long bend (Figure 1a, black open circle). Thus, advection is neglected in local dynamics. However, advection may be important in regions with varying depth, width, or curvature owing to the nonlocal (e.g., downstream or cross-gradient) adjustment of currents to variable geometry and flows (Blanckaert, 2011; Geyer, 1993; Nidzieko et al., 2009; Signell & Geyer, 1991).

The simplified depth-averaged (from equation (2)) and depth-varying momentum balances (from equation (4)) are (Kalkwijk & Booij, 1986):

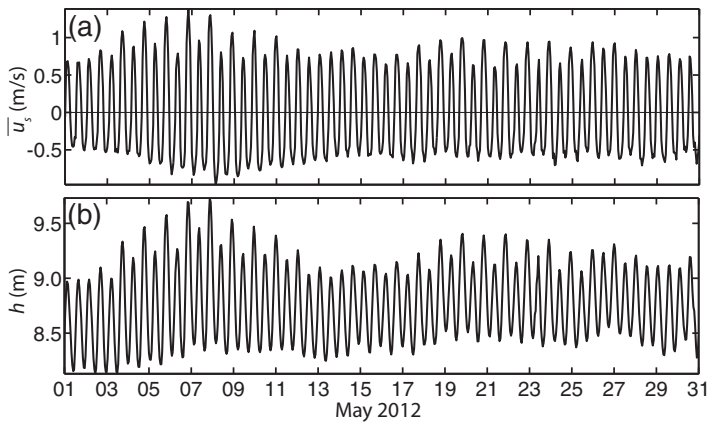$$-\frac{\overline{u_s^2}}{R} = -g\frac{\partial \eta}{\partial n} \tag{5}$$

Figure 3. (a) Depth-averaged, along-channel current $\overline{u_s}$ (the depth-averaged cross-channel current is zero by definition) and (b) water depth h in the deep channel (Figure 1a, black open circle) versus time. Along-channel current and water depth are correlated with squared correlation $r^2 = 0.8$.

$$-\frac{u_s^2 - \overline{u_s}^2}{R} = \frac{\partial}{\partial z}\left[A\frac{\partial u_n}{\partial z}\right] + \frac{\tau^{bn}}{\rho_0 h} \qquad (6)$$

4. Results and Discussion

4.1. Depth-Averaged Flows and Dynamics

Depth-averaged along-channel tidal currents in the deep channel (Figure 1a, black open circle) were flood-dominated, and ranged from -1.0 to 1.4 m/s (Figure 3a). The dominant constituent was the M2 (semidiurnal lunar) tide. The dominant overtide was the M4, which had an amplitude nearly 14% of the M2 amplitude. Although New River Inlet is a short channel relative to the tidal wavelength (the ratio of channel length to a quarter of a tidal wavelength is about 0.3) (Li & O'Donnell, 2005), the tides are progressive, with peak ebbs (floods) occurring within about 30 min of low (high) water levels (MacMahan et al., 2014) (compare Figure 3a with Figure 3b). The difference between flood and ebb water levels varied from 0.7 to 1.4 m (the latter during spring tides, Figure 3b, 7 May).

Cross-sectional-averaged peak flood and ebb flows (0.6 and -0.8 m/s, respectively) were not dissimilar on 21 May, but the horizontal structure of the along-channel flows was tidally asymmetric (Figures 4a and 4c). On flood, the flows are divided into two "jets" located in the deep (Figure 4a, red curves near along-transect distance = 0 m) and shoal (Figure 4a, red curves near along-transect distance = -120 m) channels that converge (Figure 4c, red "Flood channel jets"). On ebb, there is one jet (Figure 4a, blue curves near along-transect distance = -50 m), with weaker, divergent flow at the outer and inner banks (Figure 4c, blue "Ebb channel jet"). The depth-averaged flows at the fixed profiler are 10% and 50% smaller than the maximum channel jet flows on flood and ebb, respectively (Figure 4c, compare black arrows with maximum red and blue arrows).

The channel-scale cross-channel sea-surface tilt (Figure 4b) estimated from the GPS altitude of the boat is steeper on ebb than on flood during 21 May, similar to that estimated with the fixed pressure gages
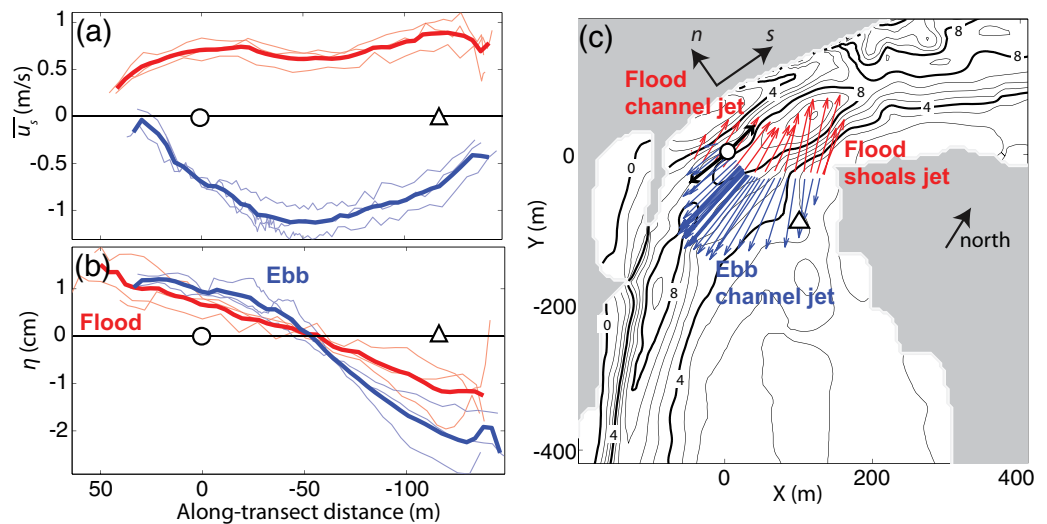

Figure 4. (a) Depth-averaged streamwise flows $\overline{u_s}$ (rotated to the local streamwise axis) and (b) the along-transect-mean-subtracted water levels η on 21 May just before, during, and just after maximum flood (thin red curves) and ebb (thin blue curves), with thick curves the corresponding averages versus along-transect distance (positive to the left (west)). (c) Boat-mounted (red and blue arrows) and fixed (black arrows) measurements of depth-averaged flows during maximum flood (red) and maximum ebb (blue) on 21 May superimposed on bathymetry (1 m depth increments with 0, 4, and 8 m contours thicker and labeled). Locations of the colocated profiler and pressure gage and the single pressure gage are indicated with the black open circle and triangle, respectively.
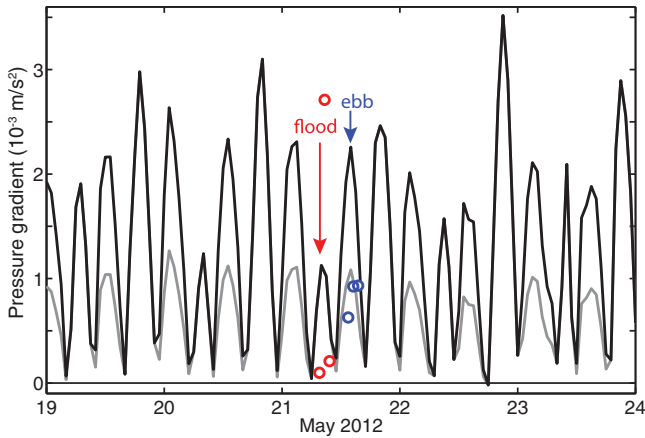
Figure 5. Cross-channel pressure gradient versus time. The circles are the GPS estimates of the pressure gradient near the profiler (Figure 4b, $17 <$ along-transect distance < -15 m) during flood (red) and ebb (blue). The curves are estimates between fixed pressure gages (Figure 4c, symbols) unweighted (black curve, estimated using processing methods described in Appendix A) and weighted (gray curve, estimated using processing methods described in Appendix A and weighing ebb results with the GPS pressure gradient estimates (blue circles)).

(Figure 5, compare peaks of black curve (the fixed estimate) near the word "flood" with peaks near "ebb"). However, there is more scatter on flood than on ebb (not shown), potentially owing to along-channel (e.g., variability in the boat transect position) and temporal variability in the pressure gradient on the flood.

There also is tidal asymmetry in the lateral structure of the water levels (Figure 4b). On ebb, the sea-surface tilt is steep over the ebb jet and inner bank (Figure 4b, thick blue curve, $-20 <$ along-transect distance < -120 m) and levels off over the weak flows on the outer bank (Figure 4b, thick blue curve, along-transect distance ≈ 0 m), whereas on flood, the average sea-surface tilt roughly is constant across the channel (Figure 4b, thick red curve). The weaker flows and tilt near the outer bank on ebb are similar to those observed in a laboratory study (Blanckaert, 2010), and may be owing to the oppositely curving bend in the channel upstream (during ebb) of the measurement transects (Figure 1c, the bend at the inland edge of the white open square). The second bend can induce centrifugal acceleration that drives momentum away from the outer bank of the downstream bend (not shown) (Blanckaert, 2010). To correct for the lateral variability in pressure gradient on ebb (the "weighted pressure gradient"), the fixed pressure gradient estimate was reduced by 52% (Figure 5, gray curve), which is the average difference between the fixed and the GPS estimates of the pressure gradient near the profiler (Figure 4b, $17 <$ along-transect distance < -15 m, and Figure 5, compare blue symbols with the black curve). On flood, no correction could be made, owing to the significant scatter in the GPS estimate of the pressure gradient near the profiler (Figure 5, compare red symbols with the black curve).

The squared correlation with centrifugal acceleration ($R = 400$ m) using the weighted pressure gradient (Figure 5, gray curve) ($r^2 = 0.86 \pm 0.07$) is higher than with the unweighted pressure gradient (Figure 5, black curve) ($r^2 = 0.65 \pm 0.13$). The weighted pressure gradient is, on average, 20% and 26% larger than the centrifugal acceleration ($R = 400$ m) during max ebbs and floods, respectively. This residual may be owing partially to the uncertainty in the radius of curvature estimate (Figure 6, linear regressions (red and blue lines) suggest radii of curvature of 320 (± 15) m on flood and 350 (± 14) m on ebb).
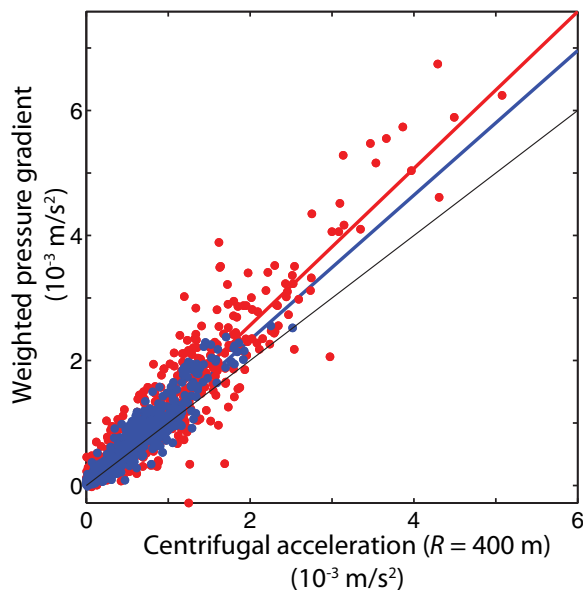
The weighted pressure gradient is less than (greater than) the driving centrifugal acceleration as the along-channel flows increase (decrease) on flood and ebb (not shown), suggesting temporal variability in the momentum balance, potentially owing to time-varying differences in the local pressure gradient or to the importance of nonlocal effects (such as along-channel or cross-channel advection (equation (4), second and third parentheses on the left-hand side)) as the flows develop (Blanckaert, 2010; Nidzieko et al., 2009). However, along-channel gradients $\partial / \partial s$ could not be resolved owing to the large distance (roughly 400 m) between in situ velocity measurements (not shown) relative to the horizontal length scales over which nonlinearity is expected to be important (section 2, 100 m) (Fong et al., 2009; Nidzieko et al., 2009; Vennell & Old, 2007). In addition, cross-channel gradients $\partial / \partial n$ could not be resolved owing to the noise in velocity measurements along the boat transect. Additional measurements are needed to resolve the importance and temporal variability of nonlocal effects (e.g., advection).

Figure 6. Weighted pressure gradient versus centrifugal acceleration ($R = 400$ m) during ebb (blue circles, slope of blue best fit line $= 1.16 \pm 0.04$) and flood (red circles, slope of red best fit line $= 1.25 \pm 0.06$). The black line is the 1:1 line.

4.2. Depth-Varying Flows and Dynamics

The along-channel flows were unidirectional (Figure 7a, red and blue curves), while the roughly 0.1–0.2 m/s cross-channel flows typically
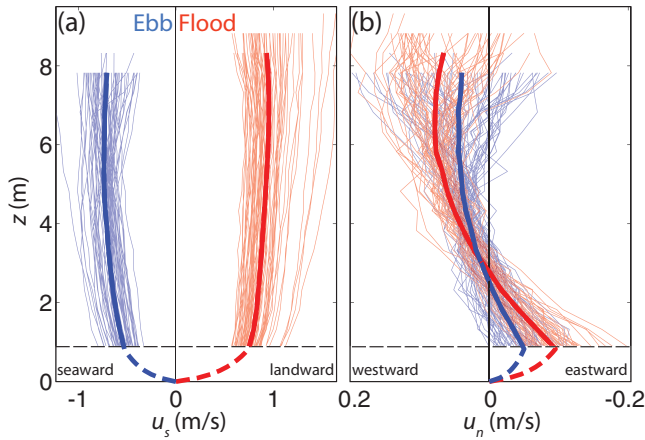
Figure 7. Distance above bottom z versus (a) along-channel u_s and (b) cross-channel u_n currents during maximum flood (red curves) and maximum ebb (blue curves) in the deep channel (Figure 1a, black open circle). The positive directions are inland (flood) and to the western bank (toward the outside of the bend). Positive is to the left in Figure 7b. The average of the individual profiles for maximum flood and ebb are shown with the thick solid red and blue curves, respectively. The horizontal dashed line is the lower limit of the measurements, and the dashed curves are examples of extrapolated flows.

had a two-layered vertical structure, with near-surface flows directed toward the outside of the bend (Figure 7b, positive direction) and near-bottom flows directed toward the inside of the bend (Figure 7b, negative direction). Sometimes the cross-channel flow structure was three-layered, with flow toward the inside of the bend (negative direction) at the surface, above the classical two-layered vertical structure (Figure 7b) (see section 4.3).

The vertical structure of the cross-channel flows at maximum flood and ebb (Figure 7b) was quantified using empirical orthogonal functions (EOFs, Emery & Thomson, 2001) (not shown). The cross-channel flows were converted into depth-normalized vertical coordinates (sigma layers), σ (defined as $\sigma = z/h$, where z is the vertical coordinate (positive upward) and h is the instantaneous profile depth) (Giddings et al., 2014; Kjerfve, 1975). Flows were divided into 10 full sigma layers and two half-sigma layers at the surface and bottom of the profile where flows are extrapolated (Kjerfve, 1975). The resulting full sigma layer sizes ranged from 0.71 to 0.85 m.

The first EOF mode, which accounted for 52% of the variance, had a root-mean-square (rms) magnitude of 0.17 m/s overall (0.20 m/s and 0.13 m/s on maximum flood and ebb, respectively) and a two-layered vertical structure. The surface (bottom) flows of the first mode were toward the outside (inside) of the bend 94% of the time, consistent with curvature-driven flow theory. The second EOF mode, which accounted for 20% of the variance, had an rms magnitude of 0.06 m/s overall (with the same magnitude on flood and ebb) and three-layered vertical structure. The direction of the circulation represented by the second mode was time-varying, with surface flows in the same direction as the cross-channel wind 66% of the time (wind effects on the subtidal flows are examined further in section 4.3).

The analytical model for curvature-driven flows (Kalkwijk & Booij, 1986) was evaluated by comparing model estimates of two-layer flow with observed two-layer flows for maximum flood and ebb during weak winds (cross-channel winds less than 2 m/s). In particular, along-channel flows in the analytical model are assumed to have a logarithmic profile proportional to the depth-averaged velocity $\overline{u_s}$ and bottom drag coefficient C_D (Kalkwijk & Booij, 1986):

$$u_{s,log} = \overline{u_s} \left[1 + \frac{\sqrt{C_D}}{\kappa} \left(1 + \ln\left(1 + \frac{z}{h} \right) \right) \right] \tag{7}$$

where κ is the von Kármán constant. The bottom drag coefficients C_D that best resolved the average along-channel flows above $z = 0.8$ m (i.e., measured flows) were 0.002 on flood (Figure 8a, gray curve) and 0.005 on ebb (Figure 8c, black curve). The ebb drag coefficient is consistent with previous studies in other parts of New River Inlet (Chen et al., 2015; Wargula et al., 2014). The corresponding eddy viscosities A are 0.03 and 0.04 m²/s on flood and ebb, consistent with the magnitude expected in unstratified systems (Geyer & Mac-Cready, 2014).

Assuming zero surface stress (no wind), steady state, negligible advective acceleration, and a parabolic eddy viscosity, the cross-channel flows may be derived analytically from the vertically varying momentum balance (equation (6)):

$$u_{n,log} = \frac{2|\overline{u_s}|h}{\kappa^2 R} f_b\left(\frac{z}{h}, \frac{\sqrt{C_D}}{\kappa} \right) \tag{8}$$

where f_b is a function of z/h and $\sqrt{C_D}/\kappa$ (see equations (17), (24), and (25) in Kalkwijk & Booij, 1986). Using a radius of curvature of 400 m (Figure 1a) and the best fit drag coefficients, the cross-channel flows were similar to the analytical model (Figures 8b and 8d, compare thick red and blue curves with gray and black curves), suggesting that a one-dimensional balance between centrifugal acceleration, diffusion, and bottom stress governs the cross-channel flows to first order. In addition, the agreement between the observations
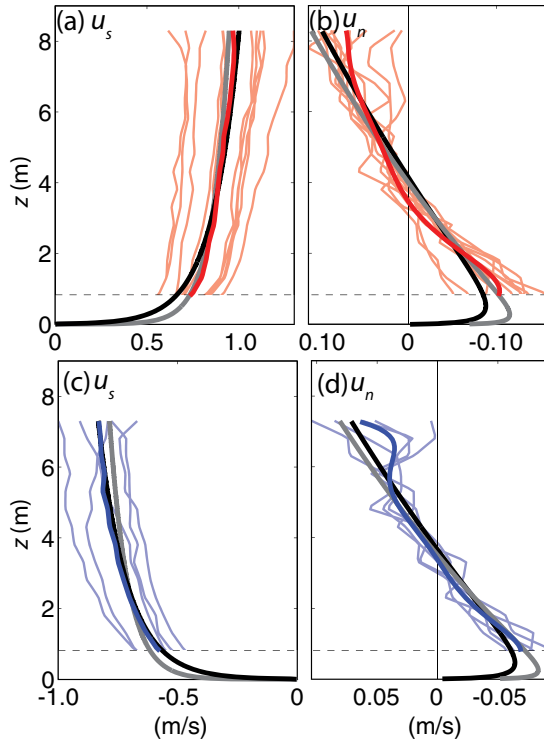
Figure 8. Distance above bottom z versus (a and c) along-channel flows u_s and (b and d) cross-channel flows u_n for (a and b) flood and (c and d) ebb. Thin curves are observations for maximum flood (red) and ebb (blue) during weak cross-channel winds ($<$2 m/s) and two-layer cross-channel flows. Thick red and blue curves are the average (the average in plots b and d are smoothed with a sixth-order polynomial fit). The dashed horizontal black line indicates the near-bottom limit of measurements. The results for the model (Kalkwijk & Booij, 1986) assuming $R = 400$ m and $C_D = 0.002$ or $C_D = 0.005$ (equations (7) and (8)) are shown by the gray and black curves, respectively.

and analytical model of the cross-channel flows is similar for different drag coefficients above the bottom boundary layer. Near-bottom flow measurements might resolve the true drag coefficient.

There is some vertical variability in the cross-channel flows that is not in the analytical model, particularly on flood. The near-bottom (near-surface) velocities and shear are larger (smaller) in the observations than in the model (Figure 8b, compare the gray with the red curves at $z \approx 1$ and 8 m). This vertical variability suggests the importance of other processes not present in the analytical model, such as a nonparabolic eddy viscosity profile (Vennell & Old, 2007) or nonlocal processes, such as advective acceleration owing to downstream adjustment of cross-channel flows to curvature (Nidzieko et al., 2009) and cross-channel gradients in cross-channel flows (Blanckaert, 2010).

4.3. Subtidal Wind-Driven Flows

To evaluate wind effects on the vertical structure of cross-channel flows, time series of the sigma-layer cross-channel flows and of the winds were detrended and low-pass filtered (cutoff period of 30 h) (Rabiner & Gold, 1975, Table 10). Results are not sensitive to cutoff periods between 25 and 40 h. The trends were added back to the cross-channel flows and winds after filtering. Low-pass filtered cross-channel flows are similar in magnitude to the tidal cross-channel flows (compare Figures 7b and 8b, 8d with Figure 9), owing to the large mean (i.e., cross-channel flows, to first order, do not change direction between flood and ebb). The low-pass filtered cross-channel flows were correlated with low-pass filtered cross-channel wind speed (Figure 9, $r^2 = 0.5$–0.7) at most sigma levels (except in the midwater column where flows change sign, and nearest the seafloor). Positive (westward) cross-channel winds corresponded to enhanced cross-channel circulation (stronger surface and near-bottom flows, Figure 9, 6–8 May) and negative (eastward) winds tended to weaken surface and bottom flows (Figure 9, 18 May) or drive opposing (negative (eastward) flows above the curvature-driven two-layered flow (Figures 7b and 9, 2–5 May).

Subtidal along-channel flows were correlated weakly with the cross-channel wind velocity at the 95% confidence level ($r^2 = 0.3$–0.5), with surface flows positive (inland-directed) and bottom flows negative (seaward) for negative (eastward) cross-channel winds (not shown). Ekman transport is unlikely to account for this effect, because the direction of change in the along-channel flows at the surface is to the left of the wind, and because the Ekman number Ek $\approx O(5)$ is large, suggesting that friction dominates over rotation.

Neither subtidal along-channel nor cross-channel flows were correlated with the along-channel component of wind at the 95% confidence level.

An idealized numerical study (Huijts et al., 2009) suggested that cross-channel wind-driven change to cross-channel currents in a straight, 3 km wide, stratified channel may be scaled by a one-dimensional balance between wind stress and vertical diffusion:

$$u_{n,\max} \approx \frac{\tau^{sn} h}{4 \rho_0 A_0} \tag{9}$$

However, using the estimated wind stress, measured tidal water depth, and $A_0 = 0.03$ m^2/s (section 4.2), the $u_{n,max}$ expected from this formula is, on average, nearly an order of magnitude smaller than the observed near-surface low-pass filtered cross-channel flows. Although the one-dimensional depth-dependent balance resolves the cross-channel flows well during low winds (section 4.2), a two-dimensional balance may be needed to explain the wind-driven change in cross-channel flows at New River Inlet.
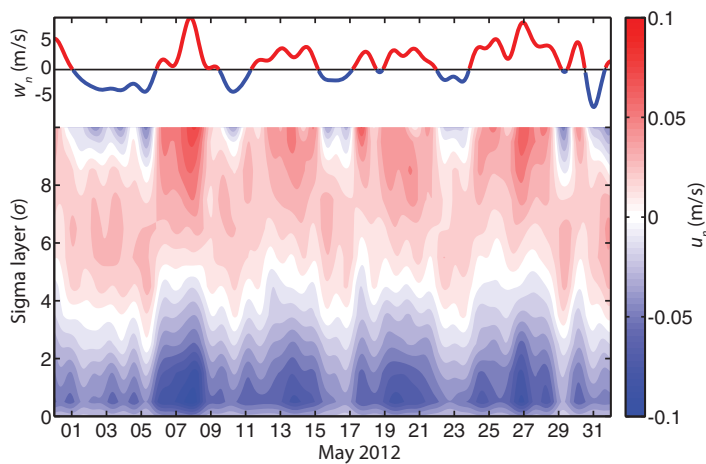
Figure 9. Low-pass filtered cross-channel wind speed w_n (red-and-blue curve) (upper y axis scale), and low-pass filtered cross-channel currents u_n (color contours, scale on the right) in the deep channel (Figure 1a, black open circle) as a function of sigma layers (lower y axis scale) versus time.

The difference between the observed flows and those estimated from equation (9) may be owing partly to underestimated wind stress. Field studies (at this site) suggest that nearshore wind stress may be 2–10 times larger than open ocean estimates (Ortiz-Suslow et al., 2015). Other factors that may explain the differences between the dynamics at New River Inlet and those described by equation (9) (Huijts et al., 2009) include the curvature ($R_{New\ River} \approx 400$ m, whereas $R_{Huijts} = \infty$ (straight)), the channel width (fetch) ($B_{New\ River} \approx 200$ m, whereas $B_{Huijts} = 3$ km), and eddy diffusivity ($A_{0,New\ River} \approx 0.03$ m²/s, suggesting well-mixed conditions, whereas $A_{0,Huijts} = 0.004$ m²/s, suggesting stratification). Other numerical simulations in an idealized straight channel without other sources (e.g., baroclinicity, curvature, Coriolis terms) of cross-channel flow forcing showed minimal cross-channel flow response to winds of any direction (Hinata et al., 2010). At New River, the effects of cross-channel winds on cross-channel flows may be enhanced by the underlying curvature-induced flows by reducing the effective water depth.

Although cross-channel wind stress often is neglected in narrow and shallow channels, observations here suggest that these winds could have a significant impact on cross-channel flows, which may affect along-channel dynamics (Lerczak & Geyer, 2004), longitudinal dispersion (Lacy & Monismith, 2001; Seim & Gregg, 1997), and bay-ocean exchange (Smith, 1976). For example, the southwesterly winds at New River Inlet may have produced three-layer flows that caused observed near-surface drifters (and potentially biota, nutrients, and other particulate matter) to move toward the inside of the bend and then to exit the inlet via the eastern "shoals" channel. Numerical model simulations did not resolve this movement of the drifters, potentially owing to a lack of resolution of the observed vertical structure of the cross-channel flows at the bend (Spydell et al., 2015).

5. Summary

Depth-averaged along-channel flows measured near the outer bank of an unstratified, narrow (150 m), shallow (8 m), 90° tidal inlet bend are stronger on flood than on ebb, coincident with a horizontal shift in the location of the channel jet. High-resolution observations of water levels across the channel suggest lateral variability and tidal asymmetry in the sea-surface tilt (the ebb tilt is mild near outer bend, but steep near the inner bend, resulting in a steeper channel-wide tilt on ebb than on flood). The depth-averaged along-channel dynamics estimated near the outer bend are consistent with a balance between the surface tilt and centrifugal acceleration.

Figure A1. Uncorrected (except for a large shift in mean on 6 May when the sensor was buried by divers) barotropic pressure gradient across the channel (Figure 1a, circle to triangle) versus time.

Two-layered and three-layered cross-channel flows were observed at the bend. The two-layered cross-channel flows during weak winds are consistent with a one-dimensional balance between centrifugal acceleration, bottom stress, and diffusion. Cross-channel wind modifies cross-channel circulation, enhancing or weakening the two-layered curvature-driven flow, as well as driving opposing flows above the curvature-driven two-layered flow, producing three-layered flow. These wind-driven changes are an order of magnitude larger than those expected from a one-dimensional balance between wind stress and vertical diffusion, suggesting the importance of two-dimensional and three-dimensional processes.

Appendix A: Pressure Gradient

There is uncertainty in the relative vertical locations of the pressure gages (Figure 1b, symbols) owing to uncertainty in the positions of the gages relative to the seafloor at initial deployment, vertical adjustments of the pressure gage on the shoals, and possible drifts in the pressure offsets (Figure 1b, black open triangle). Major jumps in water
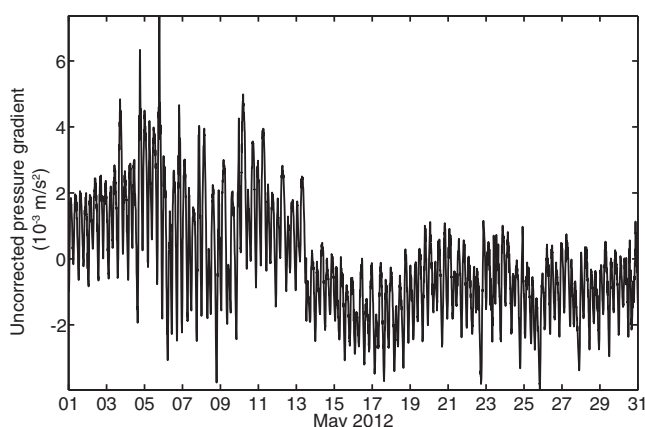
level measurements (∼60 cm) owing to known adjustments (the pressure gage on the shoals was buried by divers on 6 May, corrected in Figure A1) were corrected to within a few centimeters by comparing the mean pressure levels before and after the burial. However, the sea-surface tilt signal also varies temporally, and thus the error cannot be removed completely.

The uncorrected (except for diver adjustments) cross-channel pressure gradient has significant low frequency fluctuations ($O(10^{-3})$ m/s^2 (4–8 cm), Figure A1). Although some of the fluctuations coincide with changes in cross-channel wind direction (not shown), the low-pass filtered wind and uncorrected cross-channel pressure gradient are not correlated. Thus, the variability in the pressure gradient likely is owing to a combination of subtidal forcing (e.g., wind stress) and measurement error owing to residual adjustment errors, burial and un-burial by "natural" causes such as moving bed forms (which might affect flow-induced dynamic pressures, Raubenheimer et al., 2001), offset drifts, and fouling of the pressure gages (shells were found inside the cap of the pressure gage on the shoals). These errors are removed partially by assuming that the cross-channel pressure gradient is zero during slack (when the dominant driving force, centrifugal acceleration, is near zero, Nidzieko et al., 2009) (Figure 5, black curve). Although, this process also may remove a real signal, the main results of the tidal momentum balance analysis are qualitatively the same with and without correcting the pressure gradient.

References

Becherer, J., Stacey, M. T., Umlauf, L., & Burchard, H. (2015). Lateral circulation generates flood tide stratification and estuarine exchange flow in a curved tidal inlet. *Journal of Physical Oceanography*, 45, 638–656. https://doi.org/10.1175/JPO-D-14-0001.1

Blanckaert, K. (2010). Topographic steering, flow recirculation, velocity redistribution, and bed topography in sharp meander bends. *Water Resources Research*, 46, W09506. https://doi.org/10.1029/2009WR008303

Blanckaert, K. (2011). Hydrodynamic processes in sharp meander bends and their morphological implications. *Journal of Geophysical Research*, 116, F01003. https://doi.org/10.1029/2010JF001806

Boussinesq, J. (1868). Memoir on the influence of friction in the regular motion of fluids. *Journal De Mathématiques Pures Et Appliquées*, 2(13), 209–241.

Brown, J. M., & Wolf, J. (2009). Coupled wave and surge modelling for the eastern Irish Sea and implications for model wind-stress. *Continental Shelf Research*, 29(10), 1329–1342. https://doi.org/10.1016/j.csr.2009.03.00

Chant, R. J., & Wilson, R. E. (1997). Secondary circulation in a highly stratified estuary. *Journal of Geophysical Research*, 102(C10), 23207–23215. https://doi.org/10.1029/97JC00685

Charnock, H. (1955). Wind stress on a water surface. *Quarterly Journal of the Royal Meteorological Society*, 81, 639–640. https://doi.org/10.1002/qj.49708135027

Chen, J.-L., Hsu, T. J., Shi, F., Raubenheimer, B., & Elgar, S. (2014). Hydrodynamic modeling of New River Inlet, North Carolina using Near-CoM-TVD. *Coastal Engineering Proceedings*, 1(34), 41. https://doi.org/10.9753/icce.v3currents

Chen, J.-L., Hsu, T. J., Shi, F., Raubenheimer, B., & Elgar, S. (2015). Hydrodynamic and sediment transport modeling of New River Inlet (NC) under the interaction of tides and waves. *Journal of Geophysical Research: Oceans*, 120, 4028–4047. https://doi.org/10.1002/2014JC010425

Chen, S.-N., Sanford, L. P., & Ralston, D. K. (2009). Lateral circulation and sediment transport driven by axial winds in an idealized, partially mixed estuary. *Journal of Geophysical Research*, 114, C12006. https://doi.org/10.1029/2008JC00501

Csanady, G. T. (1973). Wind-induced barotropic motions in long lakes. *Journal of Physical Oceanography*, 3, 429–438. https://doi.org/10.1175/1520-0485(1973)003<0429:WIBMIL>2.0.CO;2

Elston, S. A. (2005). *Secondary circulation in a sinuous coastal plain estuary* (PhD dissertation). Atlanta, GA: Georgia Institute of Technology.

Emery, W. J., & Thomson, R. E. (2001). *Data analysis methods in physical oceanography* (2nd ed.). Amsterdam, the Netherlands: Elsevier Science.

Fong, D. A., Monismith, S. G., Stacey, M. T., & Burau, J. R. (2009). Turbulent stresses and secondary currents in a tidal-forced channel with significant curvature and asymmetric bed forms. *Journal of Hydraulic Engineering*, 135(3), 198–208. https://doi.org/10.1061/(ASCE)0733-9429(2009)135:3(198)

Geyer, W. R. (1993). Three-dimensional tidal flow around headlands. *Journal of Geophysical Research*, 98(C1), 955–966. https://doi.org/10.1029/92JC02270

Geyer, W. R., & MacCready, P. (2014). The estuarine circulation. *Annual Review of Fluid Mechanics*, 46, 175–197. https://doi.org/10.1146/annurev-fluid-010313-141302

Geyer, W. R., Trowbridge, J. H., & Bowden, M. M. (2000). The dynamics of a partially mixed estuary. *Journal of Physical Oceanography*, 30, 2035–2048. https://doi.org/10.1175/1520-0485(2000)030<2035:TDOAPM>2.0.CO;2

Giddings, S. N., Monismith, S. G., Fong, D. A., & Stacey, M. T. (2014). Using depth-normalized coordinates to examine mass transport residual circulation in estuaries with large tidal amplitude relative to the mean depth. *Journal of Physical Oceanography*, 44, 128–148. https://doi.org/10.1175/JPO-D-12-0201.1

Hearn, C. J., Hunter, J. R., & Heron, M. L. (1987). The effects of a deep channel on the wind-induced flushing of a shallow bay or harbor. *Journal of Geophysical Research*, 92(C4), 3913–3924. https://doi.org/10.1029/JC092iC04p03913

Hench, J. L., Blanton, B. O., & Luettich, R. A. (2002). Lateral dynamic analysis and classification of barotropic tidal inlets. *Continental Shelf Research*, 22, 2615–2631. https://doi.org/10.1016/S0278-4343(02)00117-6

Hinata, H., Kanatsu, N., & Fujii, S. (2010). Dependence of wind-driven current on wind stress direction in a small semienclosed, homogeneous rotating basin. *Journal of Physical Oceanography*, 40(7), 1488–1500. https://doi.org/10.1175/2010JPO4363.1

Huijts, K. M. H., Schuttelaars, H. M., de Swart, H. E., & Friedrichs, C. T. (2009). Analytical study of the transverse distribution of along-channel and transverse residual flows in tidal estuaries. *Continental Shelf Research*, 29(1), 89–100. https://doi.org/10.1016/j.csr.2007.09.007

Kalkwijk, J. P. T., & Booij, R. (1986). Adaptation of secondary flow in nearly-horizontal flow. *Journal of Hydraulic Research*, 24(1), 19–37. https://doi.org/10.1080/00221688609499330

Kjerfve, B. (1975). Velocity averaging in estuaries characterized by a large tidal range to depth ratio. *Estuarine and Coastal Marine Science*, *3*(3), 311–323. https://doi.org/10.1016/0302-3524(75)90031-6

Kraus, E. (1972). *Atmosphere-Ocean interaction* (275 p.). London, UK: Oxford University Press.

Lacy, J. R., & Monismith, S. G. (2001). Secondary currents in a curved, stratified, estuarine channel. *Journal of Geophysical Research: Oceans*, *106*(C12), 31283–31302. https://doi.org/10.1029/2000JC000606

Large, W., & Pond, S. (1981). Open ocean momentum flux measurements in moderate to strong winds. *Journal of Physical Oceanography*, *11*, 324–336. https://doi.org/10.1175/1520-0485(1981)011<0324:OOMFMI>2.0.CO;2

Lerczak, J. A., & Geyer, W. R. (2004). Modeling the lateral circulation in straight, stratified estuaries. *Journal of Physical Oceanography*, *34*, 1410–1428. https://doi.org/10.1175/1520-0485(2004)034<1410:MTLCIS>2.0.CO;2

Li, C., & O'donnell, J. (2005). The effect of channel length on the residual circulation in tidally dominated channels. *Journal of Physical Oceanography*, *35*, 1826–1840. https://doi.org/10.1175/JPO2801

Li, Y., & Li, M. (2012). Wind-driven lateral circulation in a stratified estuary and its effects on the along-channel flow. *Journal of Geophysical Research*, *117*, C09005. https://doi.org/10.1029/2011JC007829

MacMahan, J., van de Kreeke, J., Reniers, A., Elgar, S., Raubenheimer, B., Thornton, E., et al. (2014). Fortnightly tides and subtidal motions in a choked inlet. *Estuarine, Coastal and Shelf Science*, *150B*, 325–331. https://doi.org/10.1016/j.ecss.20103.025

MacVean, L. J., & Lacy, J. R. (2014). Interactions between waves, sediment, and turbulence on a shallow estuarine mudflat. *Journal of Geophysical Research: Oceans*, *119*, 1534–1553. https://doi.org/10.1002/2013JC009477

Mathieu, P. P., Deleersnijder, E., Cushman-Roisin, B., Beckers, J.-M., & Bolding, K. (2002). The role of topography in small well-mixed bays, with application to the lagoon of Mururoa. *Continental Shelf Research*, *22*(9), 1379–1395. https://doi.org/10.1016/S0278-4343(02)00002-X

Nidzieko, N. J., Hench, J. L., & Monismith, S. G. (2009). Lateral circulation in well-mixed and stratified estuarine flows with curvature. *Journal of Physical Oceanography*, *39*, 831–851. https://doi.org/10.1175/2008JPO4017.1

Ortiz-Suslow, D. G., Haus, B. K., Williams, N. J., Laxague, N. J. M., Reniers, A. J. H. M., & Graber, H. C. (2015). The spatial-temporal variability of air-sea momentum fluxes observed at a tidal inlet. *Journal of Geophysical Research: Oceans*, *120*, 660–676. https://doi.org/10.1002/2014JC010412

Peña, A., & Gryning, S.-E. (2008). Charnock's roughness length model and non-dimensional wind profiles over the sea. *Boundary-Layer Meteorology*, *128*, 191–203. https://doi.org/10.1007/s10546-008-9285-y

Ponte, A. L., Gutiérrez de Velasco, G., Valle-Levinson, A., Winters, K. B., & Winant, C. D. (2012). Wind-driven subinertial circulation inside a semienclosed bay in the Gulf of California. *Journal of Physical Oceanography*, *42*, 940–955. https://doi.org/10.1175/JPO-D-11-0103.1

Rabiner, L., & Gold, B. (1975). *Theory and application of digital signal processing*. Englewood Cliffs, NJ: Prentice-Hall.

Raubenheimer, B., Guza, R. T., & Elgar, S. (2001). Field observations of wave-driven setdown and setup. *Journal of Geophysical Research*, *106*, 4629–4638. https://doi.org/10.1029/2000JC000572

Rozovskii, I. L. (1957). *Flow of water in bends of open channels* (233 p.). Kiev: Academy of Sciences of the Ukrainian SSR.

Sanay, R., & Valle-Levinson, A. (2005). Wind-induced circulation in semienclosed homogeneous, rotating basins. *Journal of Physical Oceanography*, *35*, 2520–2531. https://doi.org/10.1175/JPO2831.1

Seim, H. E., & Gregg, M. C. (1997). The importance of aspiration and channel curvature in producing strong vertical mixing over a sill. *Journal of Geophysical Research*, *102*(C2), 3451–3472. https://doi.org/10.1029/96JC03415

Sempreviva, A. M., Larsen, S. E., Mortensen, N. G., & Troen, I. (1990). Response of neutral boundary layers to changes of roughness. *Boundary-Layer Meteorology*, *50*, 205–225. https://doi.org/10.1007%2FBF00120525

Signell, R., & Geyer, W. R. (1991). Transient eddy formation around headlands. *Journal of Geophysical Research: Oceans*, *96*(C2), 2561–2575. https://doi.org/10.1029/90JC02029

Smith, R. (1976). Longitudinal dispersion of a buoyant contaminant in a shallow channel. *Journal of Fluid Mechanics*, *78*, 677–688. https://doi.org/10.1017/S0022112076002681

Smith, S. D. (1980). Wind stress and heat flux over the ocean in gale force winds. *Journal of Physical Oceanography*, *10*, 709–726. https://doi.org/10.1175/1520-0485(1980)010<0709:WSAHFO>2.0.CO;2

Spydell, M. S., Feddersen, F., Olabarrieta, M., Chen, J., Guza, R. T., Raubenheimer, B., et al. (2015). Observed and modeled drifters at a tidal inlet. *Journal of Geophysical Research: Oceans*, *120*, 4825–4844. https://doi.org/10.1002/2014JC010541

Thomson, W. (1876). On the origin of windings of rivers in alluvial plains, with remarks on the flow of water round bends in pipes. *Proceedings of the Royal Society of London*, *25*, 5–8.

Vennell, R., & Old, C. (2007). High-resolution observations of the intensity of secondary circulation along a curved tidal channel. *Journal of Geophysical Research*, *112*, C11008. https://doi.org/10.1029/2006JC00376

Wargula, A., Raubenheimer, B., & Elgar, S. (2014). Wave-driven along-channel subtidal flows in a well-mixed ocean inlet. *Journal of Geophysical Research: Oceans*, *119*, 2987–3001. https://doi.org/10.1002/2014JC009839

Waterhouse, A. F., & Valle-Levinson, A. (2010). Transverse structure of subtidal flow in a weakly stratified subtropical tidal inlet. *Continental Shelf Research*, *30*, 281–292. https://doi.org/10.1016/j.csr.2009.11.008

Winant, C. D. (2004). Three-dimensional tidal flow in an elongated, rotating basin. *Journal of Physical Oceanography*, *37*(9), 2345–2362. https://doi.org/10.1175/JPO3122.1

Wong, K.-C. (1994). On the nature of transverse variability in a coastal plain estuary. *Journal of Geophysical Research*, *99*(C7), 14209–14222. https://doi.org/10.1029/94JC00861

Wong, K.-C., & Valle-Levinson, A. (2002). On the relative importance of the remote and local wind effects on the subtidal exchange at the entrance to the Chesapeake Bay. *Journal of Marine Research*, *60*(3), 477–498. https://doi.org/10.1357/002224002762231188

Xie, X., Li, M., & Boicourt, W. C. (2017). Baroclinic effects on wind-driven lateral circulation in Chesapeake Bay. *Journal of Physical Oceanography*, *47*(2), 433–445. https://doi.org/10.1175/JPO-D-15-0233.1